*Article*

# Fabrication and Application of Ag, Black TiO$_2$ and Nitrogen-Doped 3D Reduced Graphene Oxide (3D Black TiO$_2$/Ag/N@rGO) Evaporator for Efficient Steam Generation

Fisseha A. Bezza [ID], Samuel A. Iwarere [ID], Shepherd M. Tichapondwa [ID] and Evans M. N. Chirwa *[ID]

Water Utilization and Environmental Engineering Division, Department of Chemical Engineering, University of Pretoria, Pretoria 0002, South Africa
* Correspondence: evans.chirwa@up.ac.za

**Abstract:** The scarcity of fresh water, which is aggravated by rapid economic development and population growth, is a major threat to the modern world. Solar-driven interfacial desalination and steam generation is a promising strategy that localizes heat at the air-water interface through appropriate thermal management and demonstrates efficient photothermal performance. In the current study, Ag, black TiO$_2$, and nitrogen-doped 3D reduced graphene oxide (3D black TiO$_2$/Ag/N@rGO) hierarchical evaporator was fabricated, and its morphology, elemental composition, porosity, broadband solar absorption potential, photothermal performance, and interfacial desalination potential were assessed. The 3D solar evaporator showed efficient solar absorption over the entire broadband UV-visible near-infrared (UV-Vis NIR) region and demonstrated 99% photothermal conversion efficiency and potential freshwater generation of 1.43 kg·m$^{-2}$ h$^{-1}$. The specific surface area and porosity analyses demonstrated an ultrahigh specific surface area, high pore volume, and a mesoporous structure, with a predominant pore diameter of 4 nm. The strong photothermal performance can be attributed to the nitrogen doping of the rGO, which boosted the electrocatalytic and photothermal activity of the graphene through the activation of the excess free-flowing π electrons of the sp$^2$ configuration of the graphene; the broadband solar absorption potential of the black TiO$_2$; and the localized surface plasmon resonance effect of the AgNPs, which induced hot electron generation and enhanced photothermal conversion. Hence, the high photothermal conversion efficiency attained can be attributed to the synergistic photothermal performances of the individual components and the high interfacial surface area, abundant heat, and mass transfer microcavities of the 3D hierarchical porous solar absorber, offering multiple reflections of light and enhanced solar absorption. The study highlights the promising potential of the 3D evaporator for real-word interfacial desalination of seawater, helping to solve the water shortage problem sustainably.

**Keywords:** 3D solar absorber; interfacial desalination; photothermal conversion; reduced graphene oxide; broadband solar absorption

## 1. Introduction

Freshwater is a scarce resource and represents a global challenge for the 21st century, one which is exacerbated by rapid economic and population growth, lifestyle changes, industrialization, and urbanization [1]. Solar-driven desalination is a sustainable solution for global water shortage challenges, making it possible to desalinate the abundant seawater covering three quarters of the Earth's surface [2]. However, conventional solar-driven desalination technology, which utilizes volumetric heating to desalinate sea and hypersaline water, suffers from low efficiency due to the wastage of solar energy when heating the non-evaporative bulk water [3]. Recently, innovative interfacial desalination technology has been developed that localizes heat to the water–air interfacial area, avoiding the dissipation of energy to the non-evaporative bulk water and enabling highly enhanced solar-to-heat

conversion efficiency [4,5]. The solar-driven interfacial evaporation system consists of solar absorber that has efficient broadband solar absorption potential, appropriate thermal insulation system that avoids heat loss to the bulk water and localizes the solar to thermal conversion process at the liquid water interface as well as a floating structure that can concurrently maximize the evaporation rate and transfer of liquid to the evaporative surface [6]. In the interfacial solar-driven desalination process, photothermal materials are the core components and play an essential role in converting light to heat. To facilitate the real-world application of the interfacial evaporation system, the development of high-performance photothermal materials with high evaporation efficiency and a rational design for the structure of the evaporators, ensuring optimal energy management during solar steam generation, are prerequisites [7]. The ideal photothermal material for water evaporation should exhibit broadband solar absorptance (250–2500 nm) and low thermal emittance [8]. In addition to the broadband solar absorption property, the ability for rapid water-molecule transportation and a highly porous structure are imperative to facilitate water transfer to the active vapour generation site and enhance the vapor-escaping rate [8].

Photothermal materials can be broadly classified into carbon-based materials, such as black carbon, carbon nanotubes, graphite, and graphene; plasmonic metals, such as Ag and Au; and semiconductors, such as $Cu_2S$, $CuFeS_2$, and rutile or anatase $TiO_2$ [9,10]. Black carbon materials are naturally efficient broadband solar absorbers owing to the excitation and subsequent relaxation of electrons [6]. Specifically, graphene and graphene-based composites have demonstrated great potential for photothermal applications thanks to their intriguing physicochemical and mechanical properties [11]. Graphene is a single-atom-thick 2D carbon material with prominent features, including high mechanical strength, extremely high electrical and thermal conductivities, and large specific surface area (2675 $m^2$ $g^{-1}$), making it an ideal material for various applications in diverse areas, such as energy storage [12], sensors [13–15], and solar desalination [16–18]. On account of the resonant oscillation of surface plasmons and free electrons in the incident light of plasmonic metal nanoparticles such as AgNPs—which is called the localized surface plasmon resonance (LSPR) effect—plasmonic nanoparticles have very promising photothermal conversion potential [8]. The LSPR effect induces three sequential phenomena: near-field enhancement, hot electron generation, and photothermal conversion [19]. However, the extremely narrow absorption spectra of plasmonic metals fundamentally hinder their application for broadband wavelength light absorption. Hybridization of the plasmonic nanoparticles with porous and hierarchical carbon materials has been reported to enhance the evaporation efficiency through the synergistic plasmonic effect of the plasmonic nanoparticles and broadband absorbance of the carbonaceous material [20,21].

Black titanium dioxide ($bTiO_2$) is a new, narrow-band-gap photocatalyst that exploits the full solar spectrum and has applications in sustainable environmental remediation and energy harvesting [22]. $TiO_2$ has remained the photocatalyst of choice for many applications due to its low cost, low toxicity, high stability, and wide availability. However, $TiO_2$ has significant drawbacks, most notably its wide band-gap (3.0 and 3.2 eV for rutile and anatase, respectively), limiting the optical absorption of $TiO_2$ to the ultraviolet (UV) region, which only accounts for less than 5% of solar energy, leading to insufficient utilization of solar energy [23]. The $TiO_2$ band-gap problem can be effectively addressed by introducing $Ti^{3+}$ defects and oxygen vacancies into the titanium oxide lattice via hydrogenation. Hybridization of reduced graphene oxide (rGO) with black $TiO_2$ has been reported to enhance photothermal conversion efficiency synergistically [24]. Furthermore, nitrogen doping of rGO has been reported to increase its photothermal conversion and thermal absorption efficiency owing to the introduction of electrocatalytic active sites, as well as increasing the electrical conductivity and surface hydrophilicity [25]. Self-assembly of 2D graphene nanosheets into 3D graphene-based hierarchical interwoven monoliths imparts excellent photothermal conversion efficiency and interfacial desalination potential owing to the avoidance of the aggregation of 2D nanosheets, the provision of more heat and mass transfer channels, and a longer light scattering distance while maintaining graphene's high

thermal and electrical conductivity [26]. Remarkable steam generation potential for 3D grapheme-based solar absorbers has been recently reported in a number of studies [27–31]. The high steam generation and photothermal efficiency of the 3D evaporators, even beyond the theoretical light-to-vapor conversion limit, is due to the recycling of the latent heat from the condensation of the vapour generated [30]. Furthermore, hybridization of materials with various composites, including bimetallic materials, metal–organic materials, and metal–semiconductor composites, has been reported to lead to enhanced photothermal conversion efficiency owing to the synergistic merits of each component [19,32]. In the current study, a highly porous 3D black $TiO_2$, Ag, and nitrogen-doped rGO (3D black $TiO_2$/Ag/N@rGO) composite hierarchical structure was fabricated via hydrothermal reduction of a GO suspension, and its potential application for solar-driven interfacial desalination of hypersaline water was investigated.

## 2. Results

### 2.1. Structural and Morphological Analyses

The 3D black $TiO_2$/Ag/N@rGO shown in Figure 1b, was synthesized through hydrothermal reduction of GO along with the black $TiO_2$, Ag nanoparticles and Nitrogen precursor. The graphene oxide was produced following the oxidation of the graphite. GO has various oxygen-containing functional groups, such as hydroxyl, epoxy, carbonyl, and carboxyl functional groups. The presence of oxygen-containing functional groups makes graphene hydrophilic and enables its functionalization with diverse composites [33]. When the Ag nanoparticles and black $TiO_2$ powder were added and hydrothermally treated, the Ag and $TiO_2$ particles and nitrogen atoms bonded with the oxygen-containing functional groups of GO and formed a 3D monolithic network.
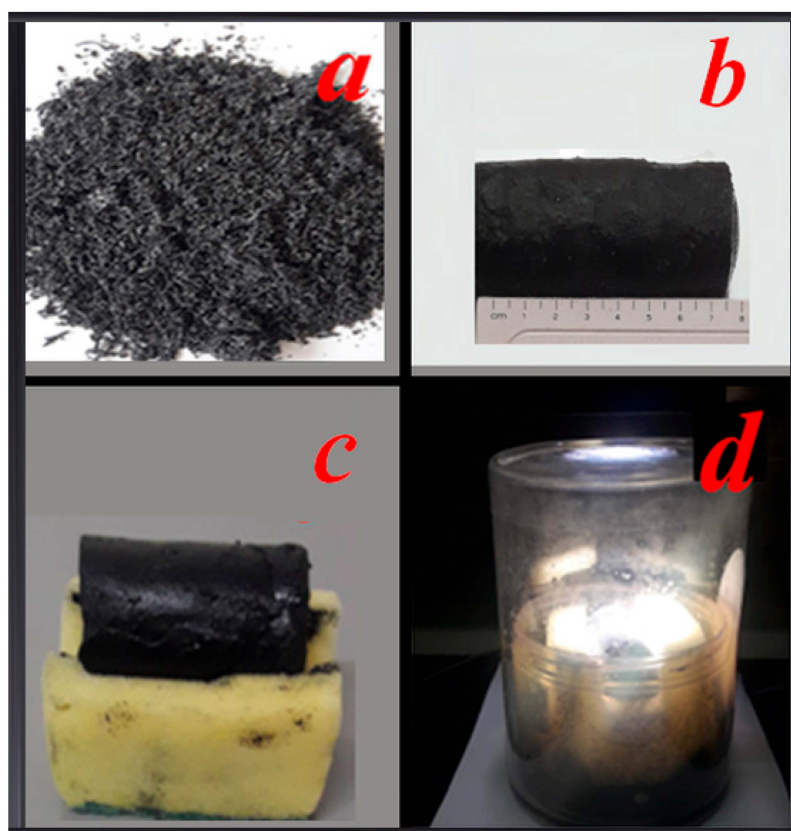


**Figure 1.** Digital images of pristine graphite (**a**); 3D black $TiO_2$/Ag/N@rGO (**b**); the cellulose sponge support and thermal insulator (**c**); and the interfacial desalination setup with the solar absorber enclosed in a transparent plastic cover to shield radiative and convective heat losses, illuminated with 1-sun solar irradiation (**d**).

The 3D monolithic structure was placed on the cellulose sponge support material. The cellulose sponge supported the 3D hierarchical monolithic structure and served as thermal insulation, helping to avoid the dissipation of heat into the bulk water. The top surface of the interfacial desalination setup was covered with transparent plastic to prevent radiative and convective heat loss into the surrounding environment. Figure 1 displays the graphite used for the synthesis of GO (a), the as-synthesised 3D black $TiO_2/Ag/N@rGO$ (b), the cellulose sponge support and thermal insulator (c) and the interfacial desalination setup with the solar absorber enclosed in a transparent plastic cover to shield the radiative and convective heat losses, illuminated with 1-sun solar irradiation (d). Figure 2 presents the schematic diagram of the overall interfacial desalination setup.
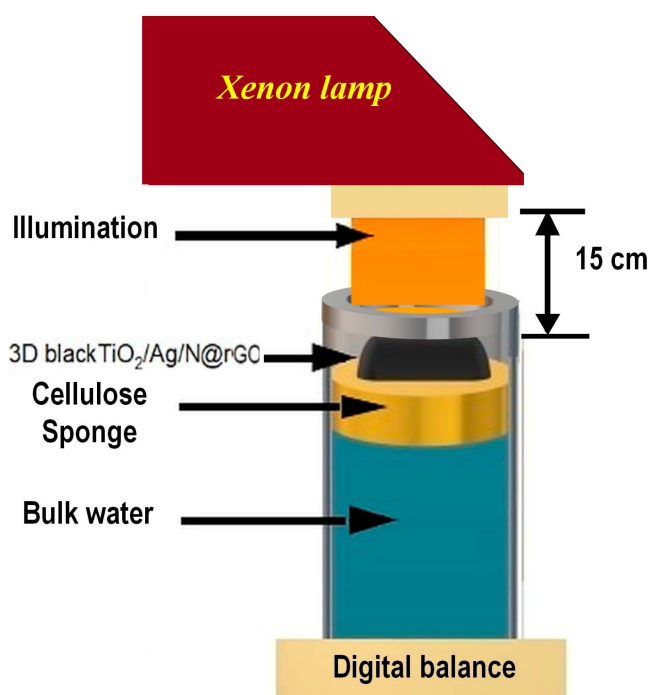


**Figure 2.** Schematic showing the solar-driven interfacial desalination setup.

A field-emission scanning electron microscopy (FESEM) study was carried out to examine the morphology and microstructure of the 3D nanocomposite. As displayed in Figure 3, highly porous, wrinkled, and fluffy morphologies were observed for both the pristine graphene (Figure 3a,b) and 3D black $TiO_2/Ag/N@rGO$ (Figure 3c,d) samples at different magnifications. A closer look at the SEM images revealed a ridged morphology with more surface defects, irregular structures, and pores on the Ag, black $TiO_2$, and nitrogen-doped rGO samples compared to the pristine graphene. This can be attributed to the defects introduced on the rGO surface due to the dopants and the loading of oxygen functional groups in the graphene sheets [34,35].

Energy-dispersive X-ray spectroscopy (EDS) analysis revealed the elemental composition of the 3D black $TiO_2/Ag/N@rGO$ sample, as shown in Figure 4. EDS elemental mapping demonstrated the uniform distribution of the dopants on the surface of the composite, as shown in Figure 5.
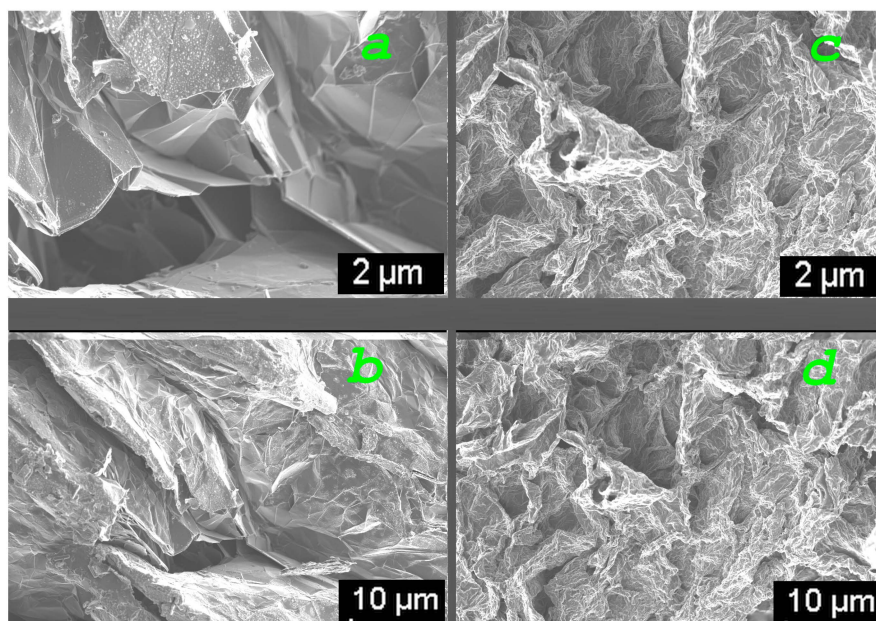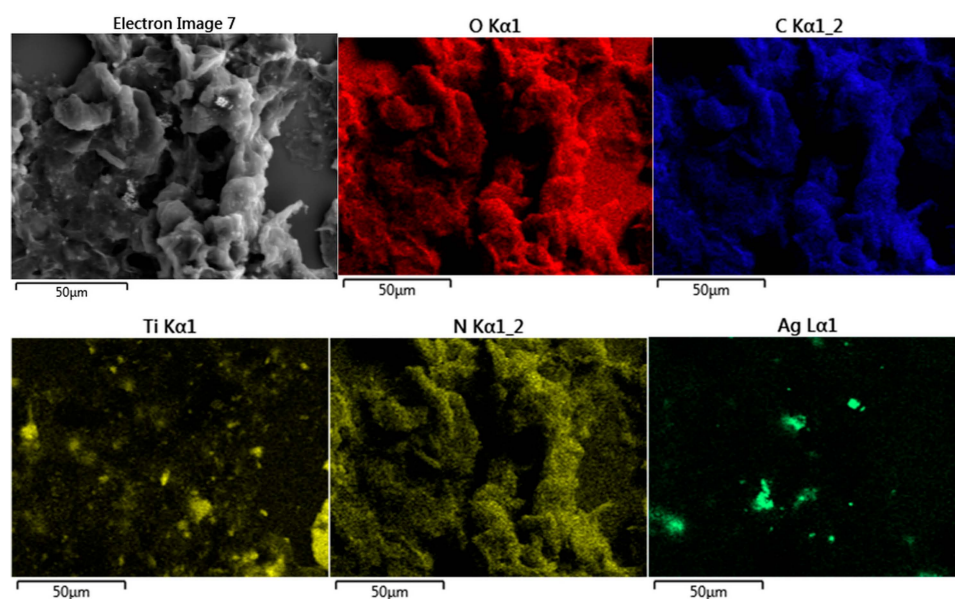
**Figure 3.** Field-emission scanning electron microscopy (FESEM) images of pristine graphene (**a**,**b**) and black TiO$_2$/Ag/N@rGO with numerous surface defects, irregular structures, and pores (**c**,**d**).
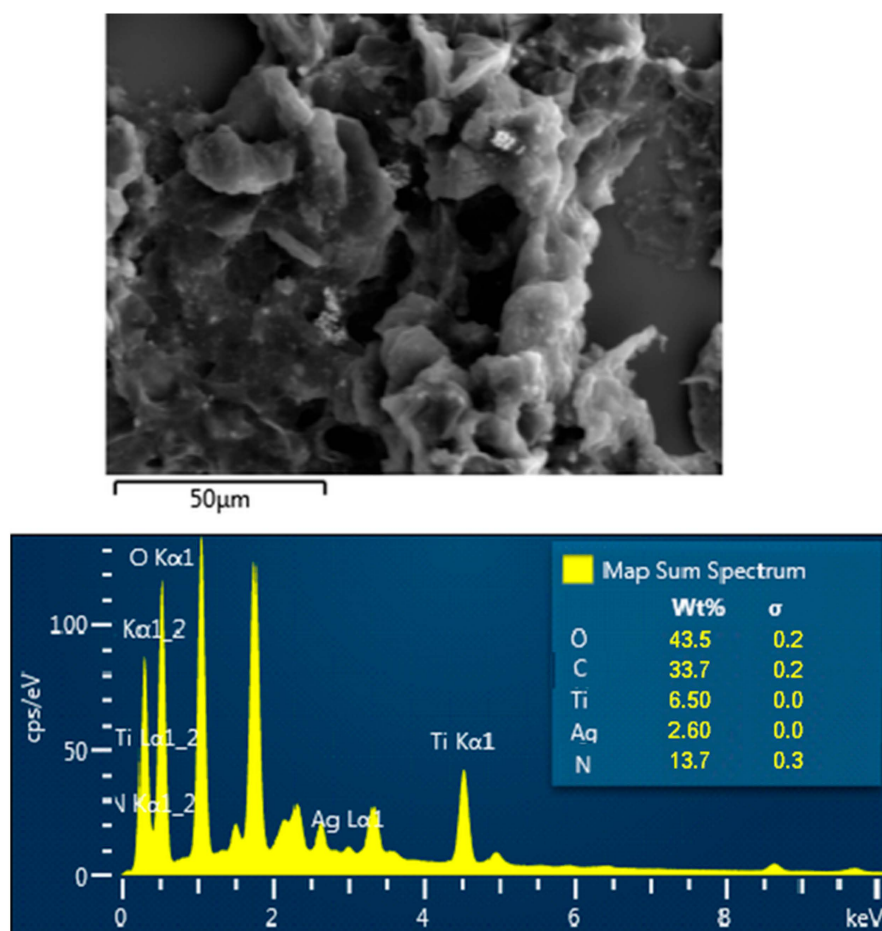


**Figure 4.** EDS elemental composition of the as-synthesized porous 3D black TiO$_2$/Ag/N@rGO sample.

**Figure 5.** EDS elemental mapping of the as-synthesized porous 3D black $TiO_2$/Ag/N@rGO sample.

2.1.1. BET Surface Area and Pore Size Distribution of the 3D Solar Absorber

Specific surface area and porosity are critical parameters for efficient capillary force-driven water transport and effective solar-to-thermal conversion. The $N_2$ adsorption–desorption isotherm of the 3D absorber at 77K and the corresponding pore size distribution curves are displayed in Figure 6a,b. The isotherm displayed a shape closest to a type IV adsorption isotherm, with a hysteresis, as defined by the IUPAC, demonstrating the presence of abundant mesopores and the predominantly mesoporous structure of the 3D solar absorber [36,37]. The BET surface area of 191.5 $m^2$/g and pore volume of 0.48 $cm^3$/g were attained based on the nitrogen adsorption–desorption isotherm. The pore size distribution obtained from the nitrogen desorption data was analysed using the density functional theory (DFT) method. As presented in Figure 6b, the particle size distribution indicated mesopores with a predominant radius of 1.73 nm. The isotherm exhibited a hysteresis from 0.4 < *P/Po* < 0.9, which is common in mesoporous materials owing to the nitrogen condensation in the pores [38]. On the other hand, the BET specific surface area of the 3D solar absorber synthesized in the absence of KOH activation was determined to be 22.37 $m^2$/g based on the nitrogen adsorption–desorption isotherm (Supplementary Materials, Figure S1). The ultra-high specific surface area and the highly porous structure were attributed to the alkaline (KOH) activation of the 3D absorber after freeze drying [39]. KOH activation of carbon materials has been reported to generate abundant micro- and mesopores owing to a series of reactions between carbon and KOH involving the formation and decomposition of $K_2CO_3$ and the gasification of other K compounds [40]. The high specific surface area provided the benefit of increasing the areal exposure of the evaporative surface and the additional advantage of increasing the microchannel for effective water transfer to the evaporative surface of the solar absorber. The high specific surface area of the 3D porous structure ensured an adequate interface between the water at the evaporative surface and the localized heat, favouring the rapid release of the vapour generated and solar–thermal energy conversion.
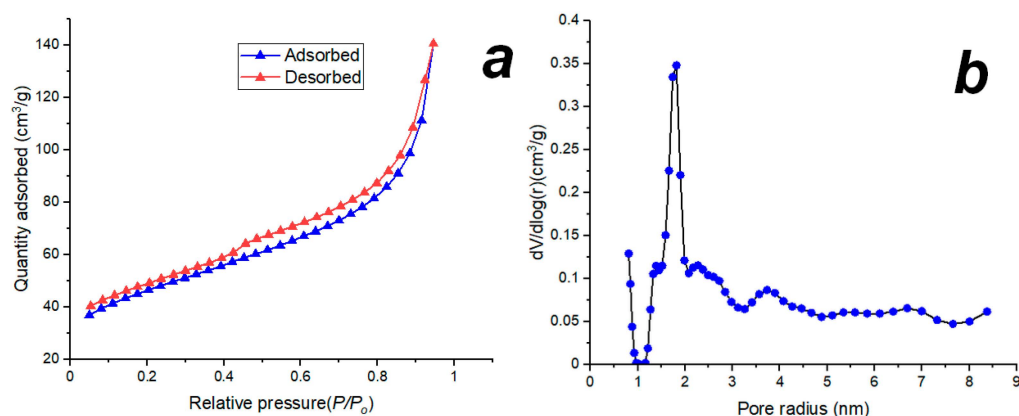
**Figure 6.** $N_2$ adsorption–desorption isotherm (**a**) and pore size distribution (**b**) for the 3D black $TiO_2/Ag/N@rGO$ material at 77K.

### 2.1.2. Fourier Transform Infrared (FTIR) Spectroscopy Analysis of the 3D Absorber

The FTIR study was carried out to examine the degree of oxidation of the graphene and to determine the oxygen-containing functional groups in the oxidized graphene compared to the pristine graphene. Oxidation of graphene imparts hydroxy (C-OH) and epoxy (C-O-C) functional groups on the basal plane and carbonyl (C=O) and carboxyl (−COOH) functional groups on the lateral plane of the graphene [41]. As depicted in Figure 7, strong peaks were observed that were ascribed to carbonyls (C=O, ~1736 cm$^{-1}$) and C=C from unoxidized graphite (1618 cm$^{-1}$) hydroxyls (−OH, ~1421 cm$^{-1}$ and a broad peak at ~3048 cm$^{-1}$) [41,42].
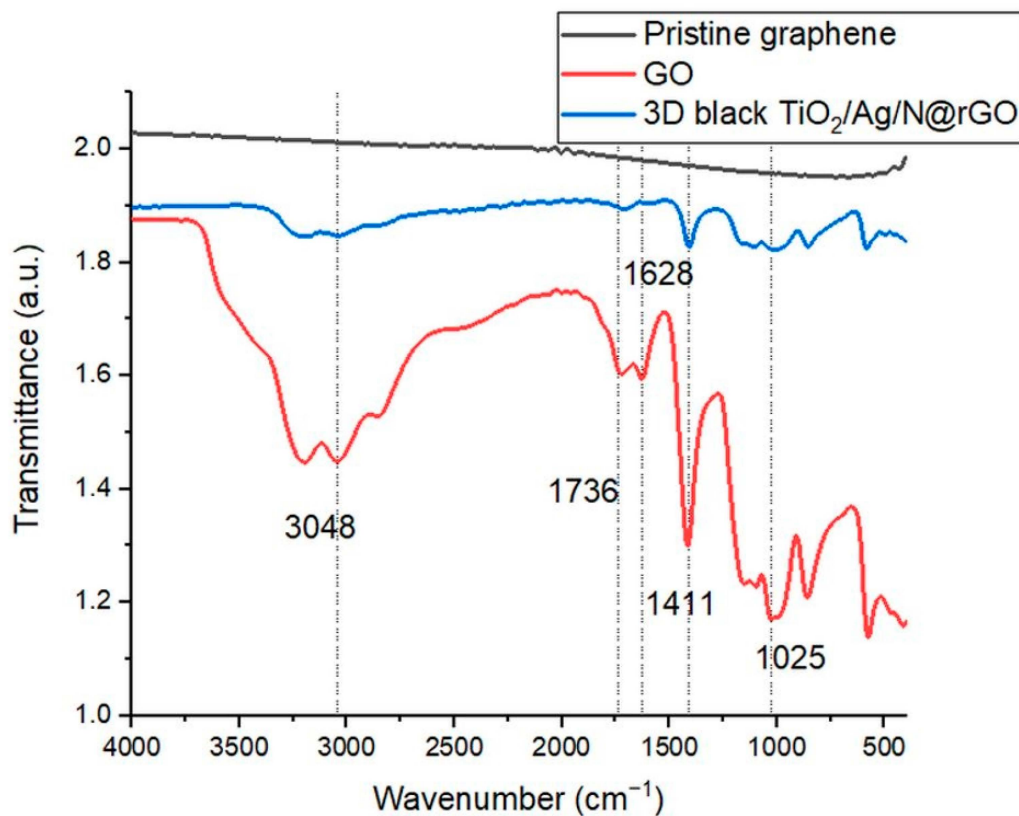


**Figure 7.** FTIR spectra of graphene oxide (GO, red), reduced graphene oxide (rGO, blue), and pristine graphene (black).

The peak at ~1025 cm$^{-1}$ was ascribed to the alkoxy C$-$O$-$C [43]. Following the reduction of the 3D absorber, there was a significant reduction in the intensity of the carbonyls (C=O, ~1736 cm$^{-1}$), hydroxyls ($-$OH, ~1421 cm$^{-1}$ and a broad peak at ~3048 cm$^{-1}$), and alkoxy C-O-C (~1025 cm$^{-1}$), confirming the reduction of GO to rGO and the restoration of sp$^2$ conjugated carbon networks. The residual oxygen in the rGO facilitated the covalent bonding of the graphene's basal and lateral plates and imparted wettability to the graphene-based composite. Oxidation of graphene disrupts the normal sp$^2$-sp$^2$ conjugated carbon network of the basal plane through a transition to tetrahedral sp$^3$ hybridization to accommodate the extra bonding for oxidation [41]. However, following the reduction, as observed in the FTIR spectra shown in Figure 7, the oxygen content was significantly reduced, and this would have significantly restored the sp$^2$ carbon–carbon network and conductivity of the graphene-based material. The residual oxygen functional groups on the reduced graphene oxide imparted hydrophilicity to the 3D absorber, enabling efficient water transfer to the evaporative area following capillary forces [40].

## 2.2. Solar Absorption Potential and Optical Absorption Property

Good broadband solar absorption performance is an important condition for efficient photothermal conversion and solar-driven water evaporation [44]. As presented in Figure 8, the 3D black TiO$_2$/Ag/N@rGO sample showed excellent broadband solar absorption over the UV–Vis NIR region compared to the GO.
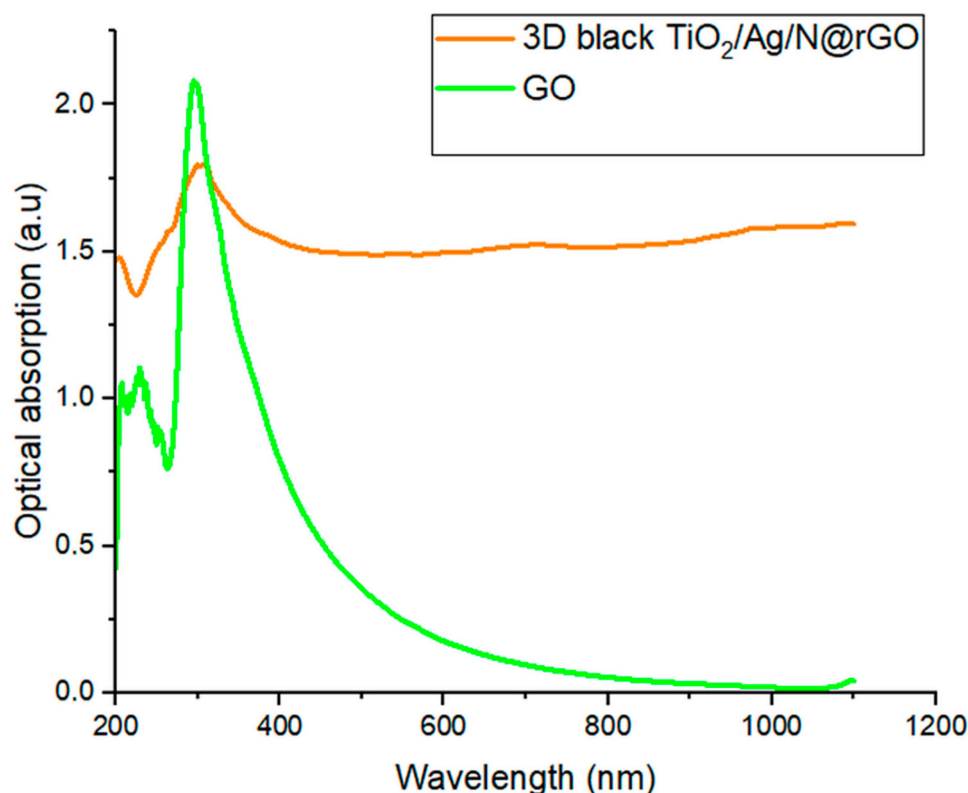


**Figure 8.** Broadband UV-Vis NIR absorption spectra for 3D black TiO$_2$/Ag/N@rGO (orange colour) and GO (green colour) samples.

Owing to the disruption of the sp$^2$ hybridized carbon network after the intercalation of the oxygen-containing functional groups, the GO functioned as a thermal insulator and showed almost no solar absorption in the visible and IR range [45]. However, following the hydrothermal reduction, the sp$^2$ hybridized conducting network was restored. The composite showed efficient solar absorption over the whole range of broadband UV-Vis NIR regions, as presented in Figure 8. The 3D black TiO$_2$/Ag/N@rGO demonstrated strong broadband solar absorption over the entirety of the UV-Vis NIR region monitored

compared to GO. Such enhanced solar absorption in the broadband solar spectra is an essential condition for efficient photothermal conversion. In the UV-Vis NIR spectra, the absorption maximum at around 229 nm represented the $\pi$-$\pi$* bond of the aromatic C-C bond, and the shoulder at ~300 nm represented the n-$\pi$* of the (C=O) bond [46]. Following the hydrothermal reduction, the peak at 300 nm disappeared, and the $\pi$-$\pi$* bond of the aromatic C-C bond redshifted to ~296 nm, indicating the reduction of GO and the restoration of the $\pi$-conjugation network within the rGO [47]. However, it should be noted that the GO was not completely reduced, and the oxygen functional groups remaining after hydrothermal reduction played an important role in tailoring the hydrophilicity of the rGO, which is an important factor for efficient photothermal conversion.

The crystallinity and phase composition of the composite material were analysed using XRD, and the results are displayed in Figure 9. The peaks demonstrated the good crystallinity of the sample. The characteristic XRD peaks at the 2$\theta$ value of 25.6° assigned to the (002) plane of the hexagonal graphene structure with an interlayer d-spacing of 3.36 Å corresponded to the rGO [48]. The diffraction peak at 43.35° with the corresponding d-spacing of 2.1 Å in the XRD pattern was assigned to the disordered turbostaic band of the rGO carbon material [49,50]. The XRD peaks at the 2$\theta$ values of 25.44°, 38.04°. 48.02°, 53.9°,55.01°, 62.41°, 68.6°, 70.01°, and 74.55° corresponded to the (101), (004), (200), (105), (211), (204), (116), (220), and (215) planes of anatase $TiO_2$ (JCPDS card no. 21-1272) [51]. The X-ray diffractograms of the sample demonstrated the presence of the anatase $TiO_2$ phase only. No diffraction peaks for Ag were identified in any of the patterns, which could have been due to the low concentration of Ag, as it was dispersed on the surface with an undetectable low concentration [52]. Nevertheless, the EDS analysis and elemental mapping confirmed the homogenous distribution of AgNPs over the entire body of the 3D rGO.
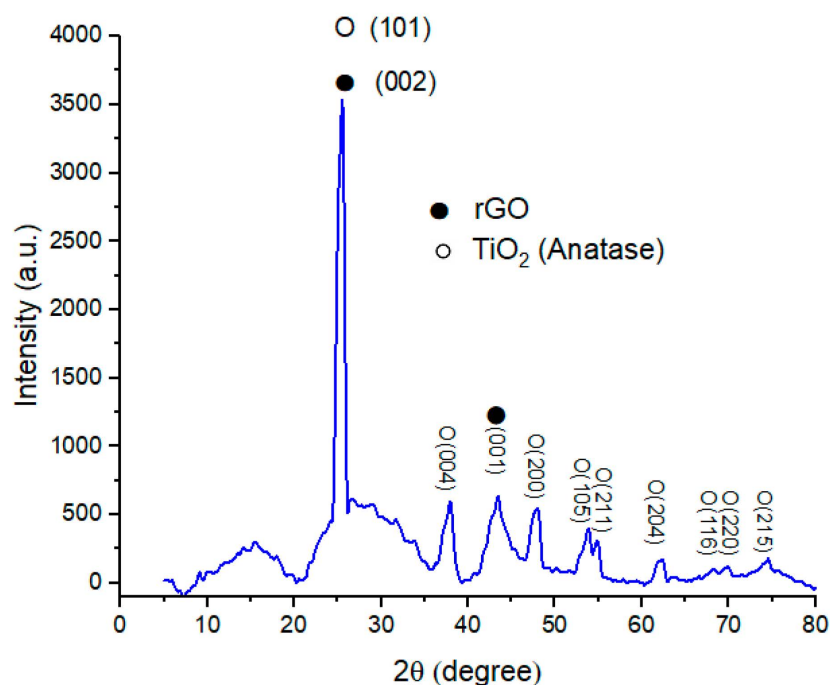


**Figure 9.** XRD pattern for the 3D black $TiO_2$/Ag/N@rGO solar absorber.

The optical performance and corresponding band gap of the black $TiO_2$ were determined and compared with the pristine $TiO_2$. As displayed in Figure 10a, the black $TiO_2$ demonstrated broadband solar absorption across the UV-Vis NIR region monitored, demonstrating its strong potential for the synergistic enhancement of the overall photothermal performance of the 3D black $TiO_2$/Ag/N@rGO solar absorber.
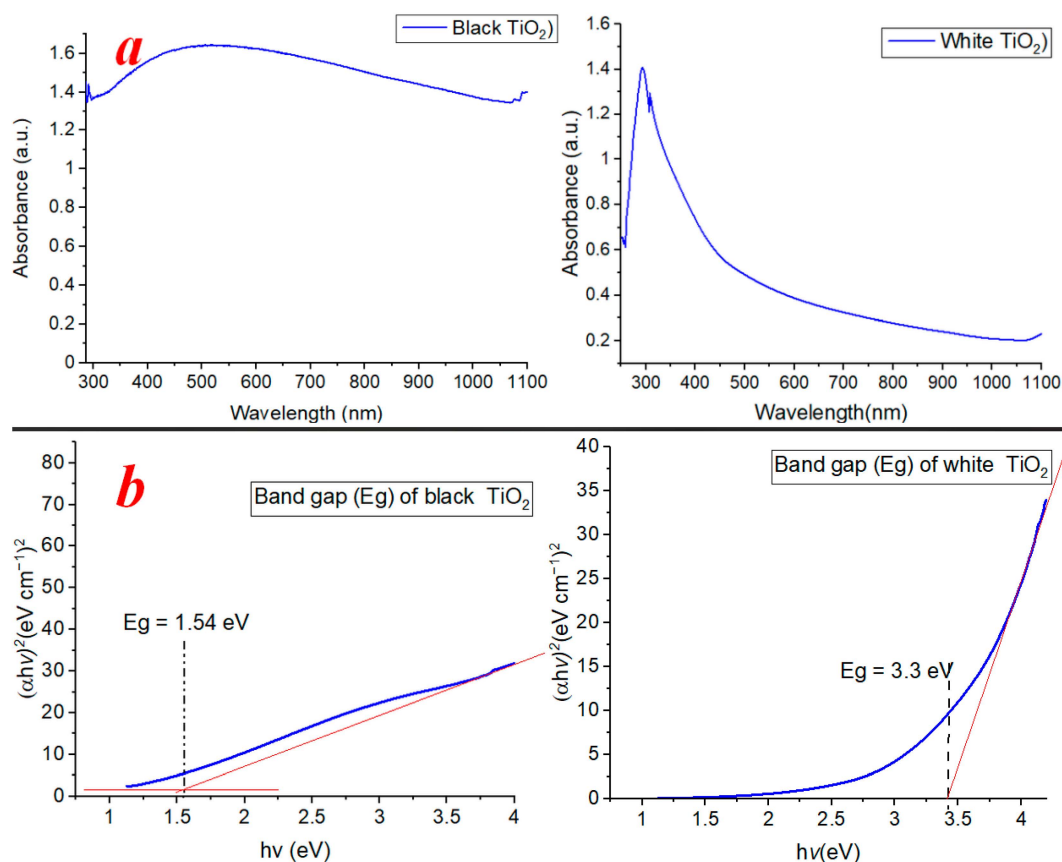
**Figure 10.** UV–Vis NIR absorption spectra (**a**) and band-gap energy (**b**) of the black $TiO_2$ and pristine $TiO_2$ estimated from their corresponding Tauc plots.

The band-gap energy of a semiconductor, which demonstrates the energy required to excite an electron from the conduction band to the valence band, can be determined using a Tauc plot generated from the relationship shown in Equation (1) [53].

$$(\alpha h\nu)^{\Upsilon} = B(h\nu - E_g) \qquad (1)$$

where $\alpha$ is the absorption coefficient, h is the Planck constant, $\nu$ is the photon's frequency, $E_g$ is the band-gap energy, and *B* is a constant. The $\gamma$ factor depends on the nature of the electron transition and is assigned values of 2 or 0.5 for direct and indirect band gaps, respectively. Figure 10b shows the Tauc plot for the direct band gap generated from the UV–Vis NIR data.

As shown in Figure 10b, the black $TiO_2$ had a band gap of ~1.54 eV, while the pristine white $TiO_2$ had a band gap of ~3.3 eV, endowing the former with broadband light absorption potential across the UV-Vis NIR region [22]. Black $TiO_2$ contains charge carrier-trapping sites within the disordered surface layer, which prevent premature charge carrier recombinations and improve its photocatalytic activity [23]. The enhanced photocatalytic performance of the black $TiO_2$ was related to the increased light absorption resulting from the introduction of lattice disorder and H-doping, which consequently narrowed the optical band gap of the black $TiO_2$ [54]. Black $TiO_2$ rGO composites have been reported to synergistically enhance photocatalytic activity through the reduction in charge carrier recombinations in black $TiO_2$ and the unique thermal and electrical conductivity properties of rGO [55]. Black titania has been reported to exhibit broadband solar absorption and excellent solar steam-generation performance [56,57].

### 2.3. Photothermal Conversion and Solar-Driven Water Evaporation Potential

The photothermal conversion efficiency and the solar-driven interfacial water vapour generation performance of the 3D absorber were explored under 1-sun illumination (1 kW/m$^2$). The photothermal performance of the 3D black TiO$_2$/Ag/N@rGO absorber was evaluated by determining the mass of the water vapour generated and monitoring the surface temperature of the absorber periodically. The interfacial saline water desalination performance and the stability of the evaporator were investigated for a total time duration of 21 h in three rounds, each consisting of 7 h. The solar-driven water evaporation flux was determined by measuring the changes in the mass of the saline water in the vessel periodically using a digital balance.

The solar-driven water evaporation rate and photothermal conversion efficiency are two crucial parameters for evaluating interfacial desalination performance [58]. The evaporation rate—the quantity of vapour generated in a unit area per unit time with a unit of kg·m$^{-2}$ h$^{-1}$—was determined using Equation (2).

$$\dot{m} = \frac{\Delta m}{S \times t} \tag{2}$$

where $\Delta m$ is the change in mass due to evaporation (kg), S is the effective absorption area (m$^2$), and $t$ refers to the solar irradiation time (h). The water vapour generated (as displayed in Figure 11) was determined to be 1.43 kg·m$^{-2}$ h$^{-1}$, while the water vapour generated in the control experiment carried out under the same conditions with no evaporator was determined to be 0.21 kg·m$^{-2}$ h$^{-1}$. The temperature of the 3D absorber was monitored using an infrared (IR) thermal imaging camera every 20 min. As observed in Figure 12, the surface temperature of the absorber increased significantly from 27.1 °C to 65.7 °C in 60 min. The 3D interconnected nanoporous structure showed remarkably good vapour generation performance compared to the control and exhibited effective salt rejection, with no salt precipitation on the surface of the evaporator throughout the entire duration of the desalination test carried out in three rounds. The effective salt rejection of the evaporator can be attributed to the nanoporous structure of the evaporator, which had a predominant pore width of 1.73 nm, functionalized with anionic oxygen-containing functional groups and the narrow interlayer spacing of the interconnected rGO nanosheets. The reduced interlayer spacing in the rGO, determined to be 3.36 Å (i.e., <7 Å), was ideal for salt rejection as it provided the potential to sieve hydrated Na$^+$ and Cl$^-$ ions [59,60]. Controlled reduction, surface functionalization, and crosslinking of GO have been observed to improve the mechanical stability and salt rejection capacity of reduced graphene oxide-based evaporators [60]. The hydroxyl, epoxy, carbonyl, and carboxyl anionic oxygen functional groups in the bases and edges of the reduced graphene oxide nanosheets reject chloride ion permeation, thereby blocking salt formation on the evaporator surface [61–63]. In addition, the nitrogen doping of the graphene nanosheets enhanced the negative charge density, which enhanced the Cl anion rejection capacity of the 3D evaporator surface, preventing salt accumulation [60,64].

The photothermal conversion efficiency $\eta$ was determined using Equation (3) [65].

$$\eta = \frac{\dot{m}.(L_v + Q)}{P_i} \tag{3}$$

where $\dot{m}$ refers to the mass flux (evaporation rate) of water; $L_v$ refers to the latent heat of the water vaporization (kJ kg$^{-1}$), which depends on the vapour temperature; Q refers to the difference in sensible heat between the initial surface temperature $T_1$ and the final surface temperature $T_2$; and $P_i$ is the incident solar power density, the value of which is1 kW·m$^{-2}$.

$$Q = C\Delta T \tag{4}$$

where C is the specific heat capacity of water (4.2 J g$^{-1}$ K$^{-1}$), $\Delta T$ refers to the increase in the temperature of the water, and $L_v$ is the vaporization enthalpy at the surface temperature.
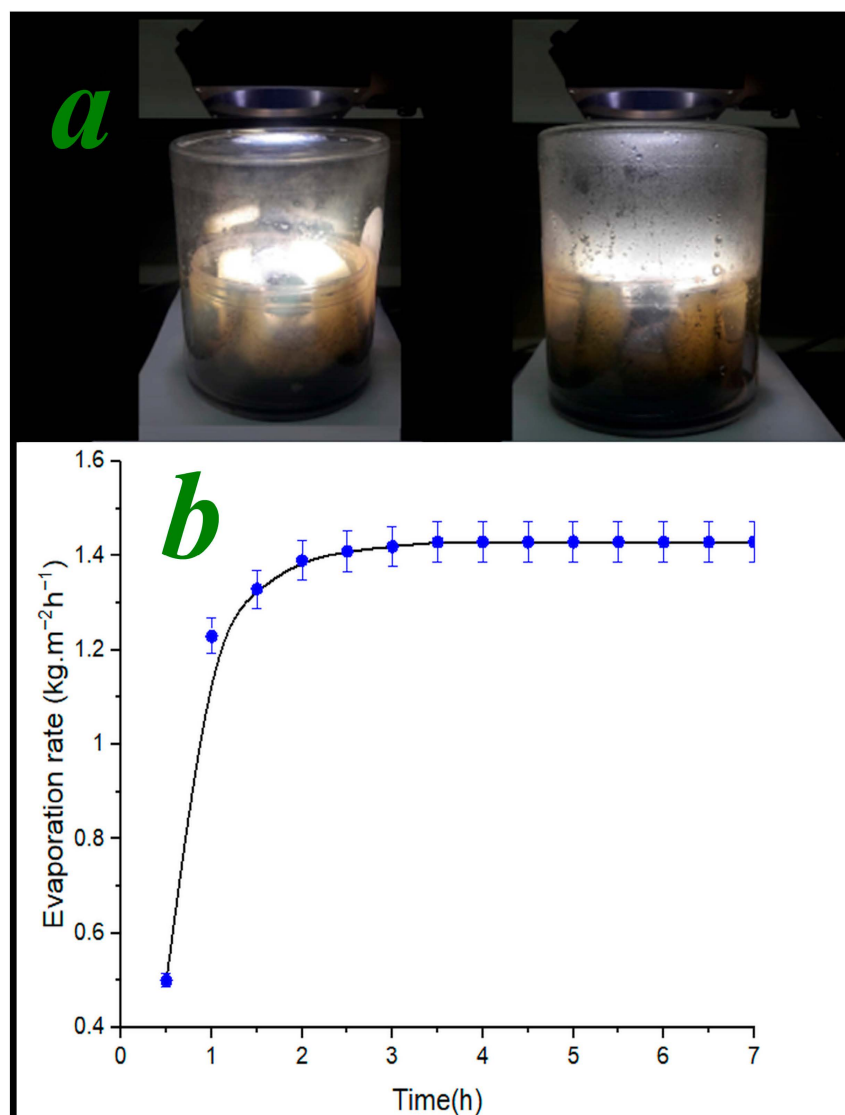
**Figure 11.** (**a**) Digital photos of the solar-driven interfacial desalination tests at the beginning of the experiment and after 30 min, respectively; (**b**) the average evaporation rate over a seven-hour experiment run in triplicate under 1-sun solar illumination.

The latent heat of water $L_v$ is 2343.6 kJ kg$^{-1}$ at 65.7 °C [66]. The photothermal conversion efficiency η was determined to be 99%. The high photothermal conversion efficiency observed can be compared to the efficacies reported in related studies [67–69]. To assess the synergistic effects of the Ag and black TiO$_2$ dopants on the overall photothermal performance of the 3D black TiO$_2$/Ag/N@rGO solar absorber, the photothermal performance of the 3D black TiO$_2$/Ag/N@rGO was compared with the photothermal performances of 3D rGO and 3D Ag@rGO obtained in our previous experiments. The studies demonstrated that, while there were no significant changes in the broadband solar absorption performance over the UV–Vis NIR region, there were considerable increases in surface temperature and steam generation potential. While the surface temperatures of the 3D rGO and 3D Ag@rGO increased from 27.1 °C to 51.6 °C and 60.1 °C, respectively, the surface temperature of the 3D black TiO$_2$/Ag/N@rGO increased from 27.1 °C to 65.7 °C. Similarly, the steam generation increased from 1.3 kg·m$^{-2}$ h$^{-1}$ to 1.41 kg·m$^{-2}$ h$^{-1}$ for the 3D rGO and 3D Ag@rGO solar absorbers and to 1.43 kg·m$^{-2}$ h$^{-1}$ for the 3D black TiO$_2$/Ag/N@rGO solar absorber, demonstrating the greater role of the dopants in enhancing the performance of the hybrid 3D solar absorbers.
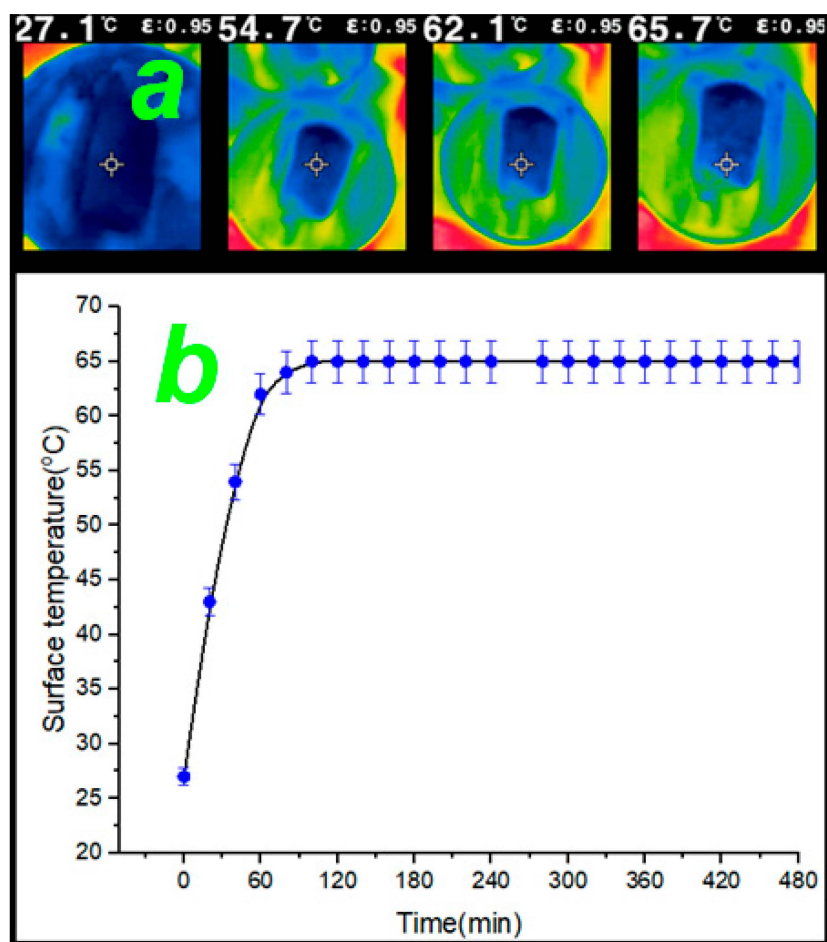
**Figure 12.** Infrared photos of the surface temperature of the 3D black $TiO_2$/Ag/N@rGO absorber under 1-sun solar illumination taken every 20 min (**a**); average surface temperature of the evaporator monitored over the entire 480 min interfacial desalination test (**b**).

## 3. Discussion

The 3D rGO-based interconnected monolithic network demonstrated remarkable photothermal performance and outstanding interfacial heating, which were ascribed to its potential for broadband solar light absorption over the full solar spectrum range, inherent porous features, large surface area, and stable mechanical strength [26]. The broadband multidirectional solar absorption of the 3D rGO hybrid with porous microstructures resulted in multiple internal reflections of light, boosting the solar absorption potential [26]. The high photothermal conversion efficiency was attributed to the synergistic photothermal performance of the AgNPs, the nitrogen doping, and the black $TiO_2$ composites used for the 3D rGO-based evaporator. Hybridization of materials, including bimetallic materials, metal–organic materials, and metal–semiconductor composites, has been reported to lead to enhanced photothermal conversion efficiency through the combination of the merits of the individual materials' optical properties [19]. Hybridization of reduced graphene oxide with plasmonic AgNPs has been reported to enhance photothermal conversion efficiency owing to the synergistic localized surface plasmon resonance effect of the AgNPs and the broadband solar absorption capacity of the rGO structure resulting from its $\pi$ electrons and high porosity [21]. Furthermore, addition of AgNPs to $TiO_2$ can form a Ag/$TiO_2$ Schottky heterojunction that inhibits the recombination of electron–hole pairs, enhancing the photothermal performance of 3D solar absorbers [51,70].

Oxygen-deficient black $TiO_2$ particles can boost the photothermal performance and electrical conductivity of 3D black $TiO_2$/Ag/N@rGO composite materials owing to their structural, electronic, and optical properties [54]. Black $TiO_2$ and rGO composites have

been reported to synergistically enhance photocatalytic activity due to the reduction in charge carrier recombination provided by the black $TiO_2$ and the unique thermal and electrical conductivity properties of rGO [55]. The hybridization of rGO with black $TiO_2$ has been reported to synergistically enhance the photothermal conversion efficiency of the composite [24]. The improved photothermal performance of the 3D absorber was also ascribed to the synergistic effect of the nitrogen doping of the rGO. As it has a comparable atomic size to carbon and five valence electrons for bonding with carbon, nitrogen has been widely used for bonding with carbon in various photothermal applications [71]. Nitrogen doping of graphene has been reported to modulate the electronic configuration, increase the conductivity, and boost the electrocatalytic and photothermal activities of graphene derivates owing to the activation of the excess free-flowing $\pi$ electrons of the $sp^2$ configuration of graphene [72]. Heteroatom doping of graphene with heteroatoms such as N, B, and P has been reported to increase the hydrophilicity of the grapheme, introduce additional electrocatalytically active sites, and increase conductivity. Hence, nitrogen activation plays a significant role in creating a defective morphology and enhancing the photothermal performance of the composite [25].

In addition to the remarkable photothermal performance of the absorber, the efficient thermal management resulted in efficient thermal insulation for the conductive heat loss to the bulk water and the radiative and convective heat losses to the external environment. The floating cellulose sponge not only served as a support material for the 3D absorber but also effectively shielded the conductive heat loss to the bulk water. The thermally insulating plastic cover on the top and lateral sides of the absorber shielded the radiative and convective heat losses. The use of a porous matrix material meant that a steady source of water could be obtained through the capillary force on the interface. The localized thermal energy was directly used to heat the water on the porous absorber surface that was transferred through the cellulose sponge via the capillary force, minimizing the heat loss to bulk water and resulting in high vapour generation and photothermal conversion efficiency. Thus, the overall remarkable solar-to-heat conversion of the 3D black $TiO_2/Ag/N@rGO$ absorber can be attributed to the synergistic effects of each component and efficient thermal management. Furthermore, the efficient salt rejection of the 3D hybrid evaporator, which is the main problem in many conventional desalination systems, significantly contributed to the stable and efficient performance of the evaporator.

Table 1 presents a comparison of evaporation flux values from various interfacial evaporation studies carried out under different solar intensities.

**Table 1.** Comparison of various evaporation fluxes from various interfacial evaporation studies carried out under different solar intensities.

| Reference | Evaporation Flux (kg·m$^{-2}$ h$^{-1}$) |
|---|---|
| [16] | 1.31 under 1 sun |
| [17] | 1.44 under 1.2 suns |
| [18] | 1.36 under 1 sun |
| [27] | From 1.42 to 1.49 under 1 sun |
| [28] | 1.37, 1.85, and 2.25 under 1 sun |
| [21] | 1.28, 2.76, 4.01, and 5.43 kg under 1, 2, 3, and 4 suns, respectively |
| [30] | 1.6 to 3.71 under 1 sun |
| [31] | 1.57 under 1 sun |
| [67] | 1.27 kg/m$^2$ h under 1 sun |
| [67] | 6.70 kg/m$^2$ h under 5 suns |
| [68] | 1, 1.1, 1.3, 1.4, and up to 2.6 under 1 sun |
| [69] | 1.62 under 1 sun |
| Current study | 1.43 under 1 sun |

## 4. Materials and Methods

### 4.1. Materials

Graphite flakes, potassium permanganate (KMnO$_4$ $\geq$99%), hydrochloric acid (HCl, 30 wt.%), sulphuric acid (H$_2$SO$_4$ > 98%), ortho-phosphoric acid (H$_3$PO$_4$ > 97%), hydrogen peroxide (H$_2$O$_2$, 30 wt.%), silver nitrate (AgNO$_3$ > 99%), Titanium oxide (Degussa P-25 > 98%), sodium boron hydride (NaBH$_4$ > 98%), and Ethylenediaminetetraacetic acid (EDTA > 98%) were purchased from Sigma Aldrich-Merck (Darmstadt, Germany).

### 4.2. Synthesis of Black TiO$_2$, Ag, and Nitrogen-Doped 3D Reduced Graphene Oxide (3D Black TiO$_2$/Ag/N@rGO)

#### 4.2.1. Synthesis of GO

Graphene oxide was synthesized using Tour's method, as described by Habte and Ayele [73]. Briefly, a mixture of 360 mL of concentrated sulphuric acid (H$_2$SO$_4$) and 40 mL of concentrated ortho-phosphoric acid (H$_3$PO$_4$) (9:1 (*v/v*) ratio) was prepared and poured into a mixture of 3.0 g graphite powder and 18 g potassium permanganate (KMnO$_4$), resulting in 40–45 °C temperature changes. The mixture was heated to 50 °C using a temperature-controlled water bath and stirred for 24 h. As the reaction continued, the mixture became pasty and muddy. After 24 h, 400 mL of ice water was added to the mixture, then 30 mL of 30 wt.% H$_2$O$_2$ was added to reduce manganese ions to soluble manganese sulphate and manganese oxides and stop the reaction. When the 30 wt.% H$_2$O$_2$ was added, a bright yellow colour was observed, indicating a high oxidation level. The resulting mixture was centrifuged (10 min at 8000 rpm), the supernatant was discarded, and the solid was washed repeatedly with HCl (30 wt.%, 200 mL) solution to remove the sulphate ions completely.

#### 4.2.2. Synthesis of Black TiO$_2$

Black TiO$_2$ was prepared using sodium boron hydride (NaBH$_4$, 98%) reduction of commercial TiO$_2$ (P25, with an anatase to rutile ratio of 80:20), with a slight modification of the previously described method [74]. In this method, 5 g of white TiO$_2$ nanoparticles was thoroughly mixed with 4 g of NaBH$_4$. Then, the mixture was placed in a porcelain boat at 500 °C for 3 h in a N$_2$ environment. The obtained product was cooled down and washed with deionized water several times, dried, powdered, and used to synthesize the 3D black TiO$_2$/Ag/N@rGO.

#### 4.2.3. Synthesis of 3D Black TiO$_2$/Ag/N@rGO

Citrate-stabilized and monodispersed Ag nanoparticles were synthesized through the reduction of AgNO$_3$ using NaBH$_4$ in the presence of trisodium citrate, as previously described by Haber and Sokolov [75]. Ethylenediaminetetraacetic acid (EDTA) was used as a nitrogen source for the nitrogen doping of the rGO. Subsequently, for the synthesis of 3D Ag, black TiO$_2$, nitrogen-doped rGO, 5 g of AgNPs, 10 g of black TiO$_2$ powder, and 20 g of EDTA components were added into a 250 mL Erlenmeyer flask containing 100 mL of 10 mg/mL GO aqueous dispersion and ultrasonicated vigorously for 15 min. The solution was then transferred to a 300 mL Teflon-lined autoclave, sealed, and heated at 180 °C (24 h) for the hydrothermal reduction of the GO suspension containing the composites. The final 3D product was freeze dried for 72 h and used for the interfacial desalination study. rGO can be considered as chemically derived graphene, the structure of which can be varied from one layer to multiple layers, with incomplete removal of oxygen atoms from the carbon structure [76]. The KOH activation process was carried out by mixing 30 mL of 5 mol/L KOH solution with the GO suspension consisting of the constituents mentioned above. Subsequently, a 3D black TiO$_2$/Ag/N@rGO monolith was obtained by freeze drying followed by thermal reduction under N$_2$, as previously described by Wang et al. [77].

### 4.3. Characterization

High-field-emission scanning electron microscopy (FESEM) coupled with energy-dispersive X-ray (EDX) analysis (EDS, JEOL-7800F, JEOL Ltd., Tokio, Japan) was carried out

to study the morphology and elemental composition of the as-synthesized samples. The broadband-diffused solar absorption performance of the GO and rGO samples was assessed over a broad wavelength range of 200–2500 nm using a UV–Vis NIR spectrophotometer (UV3600, Shimadzu Scientific Instruments, Columbia, MD, USA). For the UV–Vis NIR spectroscopy analysis, samples were prepared by dispersing the same amounts of GO and rGO in ethylene glycol with a concentration of 0.5 mg mL$^{-1}$ through 30 min of ultrasonication. The specific surface areas of the samples were measured using the dynamic Brunauer–Emmett–Teller (BET) method, and pore size distribution was analysed using density functional theory (DFT) with a N$_2$ adsorption isotherm at 180 °C collected with a Micromeritics ASAP 2000 system (Norcross, GA, USA). A Fourier Transform Infrared (FTIR) spectrometer (Perkin Elmer Spectrum 100, Waltham, MA, USA) with a spectral range of 4000–400 cm$^{-1}$, an increase of 32 scans, and a resolution of 0.2 cm$^{-1}$ was employed to detect functional groups and other molecular vibrations in the prepared samples. X-ray diffraction (XRD) analysis was carried out using a Rigaku Ultima IV X-ray diffractometer (Tokyo, Japan). with Cu-K$\alpha$ radiation ($\gamma$ = 0.154056 nm) at 40 kV and 30 mA over the 2θ range of 0 to 80°. The spacing between the reduced graphene oxide sheets (d) was determined using the Bragg equation: 2d sinθ = nλ [78], where λ is the X-ray beam wavelength (0.154 nm), d is the interlayer distance, and θ is the diffraction angle.

*4.4. Solar Steam Generation/Desalination*

The solar steam generation/desalination study was performed with the help of a xenon-arc lamp-based solar simulator (SS-X, China) under 1-sun illumination (1 kW m$^{-2}$). A cellulose sponge with a very low thermal conductivity of 0.043 W m$^{-1}$ K$^{-1}$, high hydrophilicity, and a highly porous morphology, which is beneficial for thermal insulation and rapid transfer of water [79], was procured from a local shop and used to support the 3D solar absorber. The 3D black TiO$_2$/Ag/N@rGO aerogel (7.0 × 4.5 cm) was placed on the cellulose sponge, which was floating on a saline water body within a glass basin and served as both a thermal insulating medium to shield the transfer of thermal energy to the bulk non-evaporative water and as a water propagation channel for a continuous water supply. Hence, placing the cellulose foam between the solar absorber and the bulk water, as portrayed in Figure 1, made it possible to avoid direct contact between the solar absorber and the bulk water and ensured there was a sufficient continuous water supply for the solar absorber. The whole evaporator was enclosed with a transparent polymeric cover on the top to reduce heat loss and a polypropene freshwater collector at the bottom. The condensed water flowed into the polypropene collector, and the mass change in the water in a beaker was determined using an analytical balance. Saline water with 35 wt.% NaCl was used in the desalination study to simulate high-salinity seawater. The mass of evaporated water was measured with an analytical balance (MS205DU, Mettler Toledo, Greifensee, Switzerland). An infrared (IR) camera (TG165, FLIR Systems, Portland, OR, USA) was used to monitor the surface temperature of the evaporator.

## 5. Conclusions

In contrast to conventional solar-driven water evaporation systems, which generate stream through volumetric heating of the bulk water body, the interfacial solar-driven desalination approach focusing on localization of heat at the water-air interface has demonstrated excellent photothermal conversion potential and evaporation rates. In the current work, we synthesized 3D black TiO$_2$/Ag/N@rGO, which demonstrated broadband solar absorption across the UV-Vis NIR region and good photothermal conversion performance. The absorber attained 99% photothermal conversion efficiency and 1.43 kg·m$^{-2}$ h$^{-1}$ water vapour generation. The excellent photothermal performance can be attributed to the synergistic effects of the 3D black TiO$_2$/Ag/N@rGO composite, which combined the merits of each component. The effective thermal management of the heat generated was equally vital for the observed photothermal conversion performance and vapour generation. The thermal management and efficient water transfer adjustments using the cellulose sponge

played important roles in the achievement of the observed photothermal performance. The current solar-driven interfacial desalination study demonstrates the promising potential of the 3D hybrid composite for real-world applications, making it possible to utilize inexhaustible solar energy to generate fresh water from abundant hypersaline seawater and other saline water sources and overcome the water shortage challenge facing the modern world.

# References

1. Mekonnen, M.M.; Hoekstra, A.Y. Four billion people facing severe water scarcity. *Sci. Adv.* **2016**, *2*, e1500323. [CrossRef] [PubMed]
2. Mohiuddin, S.A.; Kaviti, A.K.; Rao, T.S.; Sakthivel, S. Effect of water depth in productivity enhancement of fouling-free non-contact nanostructure desalination system. *Sustain. Energy Technol. Assess.* **2022**, *54*, 102848. [CrossRef]
3. Luo, X.; Shi, J.; Zhao, C.; Luo, Z.; Gu, X.; Bao, H. The energy efficiency of interfacial solar desalination. *Appl. Energy* **2021**, *302*, 117581. [CrossRef]
4. Lu, Y.; Fan, D.; Wang, Y.; Xu, H.; Lu, C.; Yang, X. Surface patterning of two-dimensional nanostructure-embedded photothermal hydrogels for high-yield solar steam generation. *ACS Nano* **2021**, *15*, 10366–10376. [CrossRef]
5. Wang, M.; Xu, G.; An, Z.; Xu, K.; Qi, C.; Das, R.; Zhao, H. Hierarchically structured bilayer Aerogel-based Salt-resistant solar interfacial evaporator for highly efficient seawater desalination. *Sep. Purif. Technol.* **2022**, *287*, 120534. [CrossRef]
6. Tao, P.; Ni, G.; Song, C.; Shang, W.; Wu, J.; Zhu, J.; Chen, G.; Deng, T. Solar-driven interfacial evaporation. *Nat. Energy* **2018**, *3*, 1031–1041. [CrossRef]
7. Peng, L.; Gu, X.; Yang, H.; Zheng, D.; Wang, P.; Cui, H. Ultra-high evaporation rate 3D evaporator with vertical sheets based on full use of convection flow. *J. Clean. Prod.* **2022**, *345*, 131172. [CrossRef]
8. Shi, Y.; Zhang, C.; Wang, Y.; Cui, Y.; Wang, Q.; Liu, G.; Gao, S.; Yuan, Y. Plasmonic silver nanoparticles embedded in flexible three-dimensional carbonized melamine foam with enhanced solar-driven water evaporation. *Desalination* **2021**, *507*, 115038. [CrossRef]
9. Ibrahim, I.; Seo, D.H.; McDonagh, A.M.; Shon, H.K.; Tijing, L. Semiconductor photothermal materials enabling efficient solar steam generation toward desalination and wastewater treatment. *Desalination* **2021**, *500*, 114853. [CrossRef]
10. Zang, L.; Sun, L.; Zhang, S.; Finnerty, C.; Kim, A.; Ma, J.; Mi, B. Nanofibrous hydrogel-reduced graphene oxide membranes for effective solar-driven interfacial evaporation and desalination. *Chem. Eng. J.* **2021**, *422*, 129998. [CrossRef]
11. Ali, A.; Liang, F.; Zhu, J.; Shen, P.K. The role of graphene in rechargeable lithium batteries: Synthesis, functionalisation, and perspectives. *Nano Mater. Sci.* **2022**. [CrossRef]
12. Caballero, Á.; Morales, J. Can the performance of graphene nanosheets for lithium storage in Li-ion batteries be predicted? *Nanoscale* **2012**, *4*, 2083–2092.
13. Zhang, Z.; Cai, R.; Long, F.; Wang, J. Development and application of tetrabromobisphenol A imprinted electrochemical sensor based on graphene/carbon nanotubes three-dimensional nanocomposites modified carbon electrode. *Talanta* **2015**, *134*, 435–442. [CrossRef]
14. Shangguan, Q.; Zhao, Y.; Song, Z.; Wang, J.; Yang, H.; Chen, J.; Liu, C.; Cheng, S.; Yang, W.; Yi, Z. High sensitivity active adjustable graphene absorber for refractive index sensing applications. *Diam. Relat. Mater.* **2022**, *128*, 109273. [CrossRef]

15. Shangguan, Q.; Chen, Z.; Yang, H.; Cheng, S.; Yang, W.; Yi, Z.; Wu, X.; Wang, S.; Yi, Y.; Wu, P. Design of ultra-narrow band graphene refractive index sensor. *Sensors* **2022**, *22*, 6483. [CrossRef]

16. Shi, L.; Wang, Y.; Zhang, L.; Wang, P. Rational design of a bi-layered reduced graphene oxide film on polystyrene foam for solar-driven interfacial water evaporation. *J. Mater. Chem. A* **2017**, *5*, 16212–16219. [CrossRef]

17. Yin, H.; Xie, H.; Liu, J.; Zou, X.; Liu, J. Graphene tube shaped photothermal layer for efficient solar-driven interfacial evaporation. *Desalination* **2021**, *511*, 115116. [CrossRef]

18. Yan, J.; Xiao, W.; Chen, L.; Wu, Z.; Gao, J.; Xue, H. Superhydrophilic carbon nanofiber membrane with a hierarchically macro/meso porous structure for high performance solar steam generators. *Desalination* **2021**, *516*, 115224. [CrossRef]

19. Gao, M.; Zhu, L.; Peh, C.K.; Ho, G.W. Solar absorber material and system designs for photothermal water vaporization towards clean water and energy production. *Energy Environ. Sci.* **2019**, *12*, 841–864. [CrossRef]

20. Liang, J.; Liu, H.; Yu, J.; Zhou, L.; Zhu, J. Plasmon-enhanced solar vapor generation. *Nanophotonics* **2019**, *8*, 771–786. [CrossRef]

21. Jiang, H.; Tong, L.; Liu, H.; Xu, J.; Jin, S.; Wang, C.; Hu, X.; Ye, L.; Deng, H.; Cheng, G.J. Graphene-metal-metastructure monolith via laser shock-induced thermochemical stitching of MOF crystals. *Matter* **2020**, *2*, 1535–1549. [CrossRef]

22. Andronic, L.; Enesca, A. Black $TiO_2$ synthesis by chemical reduction methods for photocatalysis applications. *Front. Chem.* **2020**, *8*, 565489. [CrossRef] [PubMed]

23. Naldoni, A.; Altomare, M.; Zoppellaro, G.; Liu, N.; Kment, S.; Zboril, R.; Schmuki, P. Photocatalysis with reduced $TiO_2$: From black $TiO_2$ to cocatalyst-free hydrogen production. *ACS Catal.* **2018**, *9*, 345–364. [CrossRef] [PubMed]

24. Liu, X.; Hou, B.; Wang, G.; Cui, Z.; Zhu, X.; Wang, X. Black titania/graphene oxide nanocomposite films with excellent photothermal property for solar steam generation. *J. Mater. Res.* **2018**, *33*, 674–684. [CrossRef]

25. Sun, H.; Wang, Y.; Liu, S.; Ge, L.; Wang, L.; Zhu, Z.; Wang, S. Facile synthesis of nitrogen doped reduced graphene oxide as a superior metal-free catalyst for oxidation. *Chem. Commun.* **2013**, *49*, 9914–9916. [CrossRef]

26. Bing, N.; Yang, J.; Zhang, Y.; Yu, W.; Wang, L.; Xie, H. 3D graphene nanofluids with high photothermal conversion and thermal transportation properties. *Sustain. Energy Fuels* **2020**, *4*, 1208–1215. [CrossRef]

27. Kim, K.; Yu, S.; An, C.; Kim, S.W.; Jang, J.H. Mesoporous three-dimensional graphene networks for highly efficient solar desalination under 1 sun illumination. *ACS Appl. Mater. Interfaces* **2018**, *10*, 15602–15608. [CrossRef]

28. Storer, D.P.; Phelps, J.L.; Wu, X.; Owens, G.; Khan, N.I.; Xu, H. Graphene and rice-straw-fiber-based 3D photothermal aerogels for highly efficient solar evaporation. *ACS Appl. Mater. Interfaces* **2020**, *12*, 15279–15287. [CrossRef]

29. Finnerty, C.T.K.; Menon, A.K.; Conway, K.M.; Lee, D.; Nelson, M.; Urban, J.J.; Sedlak, D.; Mi, B. Interfacial Solar Evaporation by a 3D Graphene Oxide Stalk for Highly Concentrated Brine Treatment. *Environ. Sci. Technol.* **2021**, *55*, 15435–15445. [CrossRef]

30. Gao, T.; Wu, X.; Owens, G.; Xu, H.L. A cobalt oxide@ polydopamine-reduced graphene oxide-based 3D photothermal evaporator for highly efficient solar steam generation. *Tungsten* **2020**, *2*, 423–432. [CrossRef]

31. Xu, H.; Lu, Y.; Jiang, F.; Zhang, J.; Ge, Y.; Li, Z. 3D porous N-doped lignosulfonate/graphene oxide aerogel for efficient solar steam generation and desalination. *Int. J. Biol. Macromol.* **2023**, *233*, 123469. [CrossRef]

32. Yang, Y.Y.; Feng, H.P.; Niu, C.G.; Huang, D.W.; Guo, H.; Liang, C.; Liu, H.Y.; Chen, S.; Tang, N.; Li, L. Constructing a plasma-based Schottky heterojunction for near-infrared-driven photothermal synergistic water disinfection: Synergetic effects and antibacterial mechanisms. *Chem. Eng. J.* **2021**, *426*, 131902. [CrossRef]

33. Adeel, M.; Bilal, M.; Rasheed, T.; Sharma, A.; Iqbal, H.M. Graphene and graphene oxide: Functionalization and nano-bio-catalytic system for enzyme immobilization and biotechnological perspective. *Int. J. Biol. Macromol.* **2018**, *120*, 1430–1440. [CrossRef]

34. Gupta, B.; Kumar, N.; Panda, K.; Kanan, V.; Joshi, S.; Visoly-Fisher, I. Role of oxygen functional groups in reduced graphene oxide for lubrication. *Sci. Rep.* **2017**, *7*, 45030. [CrossRef]

35. Pan, H.; Zhao, X.; Fu, Z.; Tu, W.; Fang, P.; Zhang, H. Visible-light induced photocatalysis of AgCl@Ag/titanate nanotubes/nitrogen-doped reduced graphite oxide composites. *Appl. Surf. Sci.* **2018**, *442*, 547–555. [CrossRef]

36. Serafin, J.; Ouzzine, M.; Junior, O.F.C.; Sreńscek-Nazzal, J. Preparation of low-cost activated carbons from amazonian nutshells for $CO_2$ storage. *Biomass Bioenergy* **2021**, *144*, 105925. [CrossRef]

37. Yilmaz, M.S. Graphene oxide/hollow mesoporous silica composite for selective adsorption of methylene blue. *Microporous Mesoporous Mater.* **2022**, *330*, 111570. [CrossRef]

38. Morsi, R.E.; Mohamed, R.S. Nanostructured mesoporous silica: Influence of the preparation conditions on the physical-surface properties for efficient organic dye uptake. *R. Soc. Open Sci.* **2018**, *5*, 172021. [CrossRef]

39. Chun, S.E.; Whitacre, J.F. Formation of micro/mesopores during chemical activation in tailor-made nongraphitic carbons. *Microporous Mesoporous Mater.* **2017**, *251*, 34–41. [CrossRef]

40. Chen, W.; Luo, M.; Yang, K.; Zhou, X. Microwave-assisted KOH activation from lignin into hierarchically porous carbon with super high specific surface area by utilizing the dual roles of inorganic salts: Microwave absorber and porogen. *Microporous Mesoporous Mater.* **2020**, *300*, 110178. [CrossRef]

41. Tarannum, F.; Muthaiah, R.; Danayat, S.; Foley, K.; Annam, R.S.; Walters, K.B.; Garg, J. Chemically Edge-Carboxylated Graphene Enhances the Thermal Conductivity of Polyetherimide–Graphene Nanocomposites. *ACS Appl. Mater. Interfaces* **2022**, *14*, 14753–14763. [CrossRef] [PubMed]

42. Xiang, C.; Wang, C.; Guo, R.; Lan, J.; Lin, S.; Jiang, S.; Lai, X.; Zhang, Y.; Xiao, H. Synthesis of carboxymethyl cellulose-reduced graphene oxide aerogel for efficient removal of organic liquids and dyes. *J. Mater. Sci.* **2019**, *54*, 1872–1883. [CrossRef]

43. Xu, Y.; Fleischer, A.S.; Feng, G. Reinforcement and shape stabilization of phase-change material via graphene oxide aerogel. *Carbon* **2017**, *114*, 334–346. [CrossRef]

44. Wang, Y.; Wang, C.; Song, X.; Huang, M.; Megarajan, S.K.; Shaukat, S.F.; Jiang, H. Improved light-harvesting and thermal management for efficient solar-driven water evaporation using 3D photothermal cones. *J. Mater. Chem. A* **2018**, *6*, 9874–9881. [CrossRef]

45. Cui, P.; Xue, Y. Tuning nonradiative recombination loss by selective oxidation patterns of epoxy groups bound to different sites of graphene quantum dots. *Chem. Eng. J.* **2022**, *431*, 134052. [CrossRef]

46. Rabchinskii, M.K.; Shnitov, V.V.; Dideikin, A.T.; Aleksenskii, A.E.; Vul', S.P.; Baidakova, M.V.; Pronin, I.I.; Kirilenko, D.A.; Brunkov, P.N.; Weise, J.; et al. Nanoscale perforation of graphene oxide during photoreduction process in the argon atmosphere. *J. Phys. Chem. C* **2016**, *120*, 28261–28269. [CrossRef]

47. Zhang, P.; Wang, H.; Zhang, X.; Xu, W.; Li, Y.; Li, Q.; Wei, G.; Su, Z. Graphene film doped with silver nanoparticles: Self-assembly formation, structural characterizations, antibacterial ability, and biocompatibility. *Biomater. Sci.* **2015**, *3*, 852–860. [CrossRef]

48. Bagheri, S.; Jamal, N.; Halilu, A.; TermehYousefi, A. Novel rGO-TC (n) Nanosheets developed via click chemistry as a lubricant anti-wear additive. *Sci. Rep.* **2018**, *8*, 1–9. [CrossRef]

49. Xu, Z.; Huang, Y.; Min, C.; Chen, L.; Chen, L. Effect of $\gamma$-ray ra-diation on the polyacrylonitrile based carbon fibers. *Radiat. Phys. Chem.* **2010**, *79*, 839–843. [CrossRef]

50. Yusoff, N.; Rameshkumar, P.; Shahid, M.M.; Huang, S.T.; Huang, N.M. Amperometric detection of nitric oxide using a glassy carbon electrode modified with gold nanoparticles incorporated into a nanohybrid composed of reduced graphene oxide and Nafion. *Microchim. Acta* **2017**, *184*, 3291–3299. [CrossRef]

51. Li, Z.; Haidry, A.A.; Liu, Y.; Sun, L.; Xie, L.; Fatima, Q.; Yao, Z. Strongly coupled $Ag/TiO_2$ heterojunction: From one-step facile synthesis to effective and stable ethanol sensing performances. *J. Mater. Sci. Mater. Electron.* **2018**, *29*, 19219–19227. [CrossRef]

52. Dong, P.; Yang, F.; Cheng, X.; Huang, Z.; Nie, X.; Xiao, Y.; Zhang, X. Plasmon enhanced photocatalytic and antimicrobial activities of $Ag-TiO_2$ nanocomposites under visible light irradiation prepared by DBD cold plasma treatment. *Mater. Sci. Eng. C* **2019**, *96*, 197–204. [CrossRef] [PubMed]

53. Makuła, P.; Pacia, M.; Macyk, W. How to correctly determine the band gap energy of modified semiconductor photocatalysts based on UV–Vis spectra. *J. Phys. Chem. Lett.* **2018**, *9*, 6814–6817. [CrossRef]

54. Xin, X.; Xu, T.; Wang, L.; Wang, C. $Ti^{3+}$-self doped brookite $TiO_2$ single-crystalline nanosheets with high solar absorption and excellent photocatalytic $CO_2$ reduction. *Sci. Rep.* **2016**, *6*, 23684. [CrossRef]

55. Shafiee, A.; Aibaghi, B.; Carrier, A.J.; Ehsan, M.F.; Nganou, C.; Zhang, X.; Oakes, K.D. Rapid photodegradation mechanism enabled by broad-spectrum absorbing black anatase and reduced graphene oxide nanocomposites. *Appl. Surf. Sci.* **2022**, *575*, 151718. [CrossRef]

56. Zhu, G.; Xu, J.; Zhao, W.; Huang, F. Constructing black titania with unique nanocage structure for solar desalination. *ACS Appl. Mater. Interfaces* **2016**, *8*, 31716–31721. [CrossRef]

57. Ye, M.; Jia, J.; Wu, Z.; Qian, C.; Chen, R.; O'Brien, P.G.; Sun, W.; Dong, Y.; Ozin, G.A. Synthesis of black TiOx nanoparticles by Mg reduction of $TiO_2$ nanocrystals and their application for solar water evaporation. *Adv. Energy Mater.* **2017**, *7*, 1601811. [CrossRef]

58. Han, X.; Besteiro, L.V.; Koh, C.S.L.; Lee, H.K.; Phang, I.Y.; Phan-Quang, G.C.; Ng, J.Y.; Sim, H.Y.F.; Lay, C.L.; Govorov, A.; et al. Intensifying heat using MOF-isolated graphene for solar-driven seawater desalination at 98% solar-to-thermal efficiency. *Adv. Funct. Mater.* **2021**, *31*, 2008904. [CrossRef]

59. Mi, B. Graphene oxide membranes for ionic and molecular sieving. *Science* **2014**, *343*, 740–742. [CrossRef]

60. Anand, A.; Unnikrishnan, B.; Mao, J.Y.; Lin, H.J.; Huang, C.C. Graphene-based nanofiltration membranes for improving salt rejection, water flux and antifouling—A review. *Desalination* **2018**, *429*, 119–133. [CrossRef]

61. Liu, G.; Jin, W.; Xu, N. Graphene-based membranes. *Chem. Soc. Rev.* **2015**, *44*, 5016–5030. [CrossRef] [PubMed]

62. Konatham, D.; Yu, J.; Ho, T.A.; Striolo, A. Simulation insights for graphene-based water desalination membranes. *Langmuir* **2013**, *29*, 11884–11897. [CrossRef] [PubMed]

63. Rahiminejad, M.; Mortazavi, V.; Moosavi, A.; Nouri-Borujerdi, A. Transport of Water Contaminated with Various Ions Through Nanoporous Graphene: A Molecular Dynamics Simulation. *Transp. Porous Media* **2022**, *146*, 537–557. [CrossRef]

64. Salahshoor, Z.; Shahbazi, A.; Koutahzadeh, N. Developing a novel nitrogen-doped hollow porous carbon sphere (N-HPCS) blended nanofiltration membrane with superior water permeance characteristic for high saline and colored wastewaters treatment. *Chem. Eng. J.* **2022**, *431*, 134068. [CrossRef]

65. Ghasemi, H.; Ni, G.; Marconnet, A.M.; Loomis, J.; Yerci, S.; Miljkovic, N.; Chen, G. Solar steam generation by heat localization. *Nat. Commun.* **2014**, *5*, 4449. [CrossRef]

66. Available online: https://www.engineeringtoolbox.com/water-properties-d_1573.html (accessed on 1 December 2022).

67. Ming, X.; Guo, A.; Zhang, Q.; Guo, Z.; Yu, F.; Hou, B.; Wang, Y.; Homewood, K.P.; Wang, X. 3D macroscopic graphene oxide/MXene architectures for multifunctional water purification. *Carbon* **2020**, *167*, 285–295. [CrossRef]

68. Wei, C.; Zhang, X.; Ma, S.; Zhang, C.; Li, Y.; Chen, D.; Jiang, H.; Xu, Z.; Huang, X. Ultra-robust vertically aligned three-dimensional (3D) Janus hollow fiber membranes for interfacial solar-driven steam generation with salt-resistant and multi-media purification. *Chem. Eng. J.* **2021**, *425*, 130118. [CrossRef]

69. Lei, Z.; Sun, X.; Zhu, S.; Dong, K.; Liu, X.; Wang, L.; Zhang, X.; Qu, L.; Zhang, X. Nature inspired MXene-decorated 3D honeycomb-fabric architectures toward efficient water desalination and salt harvesting. *Nano-Micro Lett.* **2022**, *14*, 10. [CrossRef]

70.    Hong, D.; Lyu, L.M.; Koga, K.; Shimoyama, Y.; Kon, Y. Plasmonic Ag@ TiO2 core–shell nanoparticles for enhanced $CO_2$ photoconversion to CH4. *ACS Sust Chem. Eng.* **2019**, *7*, 18955–18964. [CrossRef]

71.    Li, X.; Zhu, X.; Zhu, Y.; Yuan, Z.; Si, L.; Qian, Y. Porous nitrogen-doped carbon vegetable-sponges with enhanced lithium storage performance. *Carbon* **2014**, *69*, 515–524. [CrossRef]

72.    Zhao, Y.; Yang, L.; Chen, S.; Wang, X.; Ma, Y.; Wu, Q.; Jiang, Y.; Qian, W.; Hu, Z. Can boron and nitrogen co-doping improve oxygen reduction reaction activity of carbon nanotubes? *J. Am. Chem. Soc.* **2013**, *135*, 1201–1204. [CrossRef]

73.    Habte, A.T.; Ayele, D.W. Synthesis and characterization of reduced graphene oxide (rGO) started from graphene oxide (GO) using the tour method with different parameters. *Adv. Mater. Sci. Eng.* **2019**, *5058163*, 1–9. [CrossRef]

74.    Shen, L.; Xing, Z.; Zou, J.; Li, Z.; Wu, X.; Zhang, Y.; Zhu, Q.; Yang, S.; Zhou, W. Black TiO2 nanobelts/g-C3N4 nanosheets laminated heterojunctions with efficient visible-light-driven photocatalytic performance. *Sci. Rep.* **2017**, *7*, 41978. [CrossRef]

75.    Haber, J.; Sokolov, K. Synthesis of stable citrate-capped silver nanoprisms. *Langmuir* **2017**, *33*, 10525–10530. [CrossRef]

76.    Le, G.T.; Manyam, J.; Opaprakasit, P.; Chanlek, N.; Grisdanurak, N.; Sreearunothai, P. Divergent mechanisms for thermal reduction of graphene oxide and their highly different ion affinities. *Diam. Relat. Mater.* **2018**, *89*, 246–256. [CrossRef]

77.    Wang, S.; Tristan, F.; Minami, D.; Fujimori, T.; Cruz-Silva, R.; Terrones, M.; Takeuchi, K.; Teshima, K.; Rodríguez-Reinoso, F.; Endo, M.; et al. Activation routes for high surface area graphene monoliths from graphene oxide colloids. *Carbon* **2014**, *76*, 220–231. [CrossRef]

78.    Ho, C.Y.; Wang, H.W. Characteristics of thermally reduced graphene oxide and applied for dye-sensitized solar cell counter electrode. *Appl. Surf. Sci.* **2015**, *357*, 147–154. [CrossRef]

79.    Liu, J.; Liu, Q.; Ma, D.; Yuan, Y.; Yao, J.; Zhang, W.; Su, H.; Su, Y.; Gu, J.; Zhang, D. Simultaneously achieving thermal insulation and rapid water transport in sugarcane stems for efficient solar steam generation. *J. Mater. Chem. A* **2019**, *7*, 9034–9039. [CrossRef]